RESEARCH ARTICLE

Optimization of 3D Printing Parameters of Biodegradable Polylactic Acid/Hydroxyapatite Composite Bone Plates

Patiguli Aihemaiti, Houfeng Jiang, Wurikaixi Aiyiti*, Ayiguli Kasimu

School of Mechanical Engineering, Xinjiang University, Urumqi 830000, PR China

Abstract: The building parameters of three-dimensional (3D) printed polylactic acid/hydroxyapatite (HA) composite bone plates were optimized by an orthogonal experiment, and the effects of the layer thickness, printing speed, filament feeding speed, and HA content on the bending strengths of the specimens were analyzed. The deformation characteristics of the specimens were studied by 3D full-field strain analysis, and the internal defects of the specimens were analyzed. The effects of different combinations of the process parameters on the cross-sectional shape of the single deposited line, printing temperature, and pressure of the molten material were further analyzed. The results showed that the factors affecting the bending properties were the layer thickness, printing speed, filament feeding speed, and HA content, successively. The optimized process parameters were an HA content of 10%, a layer thickness of 0.1 mm, a printing speed of 30 mm/s, and a filament feeding speed of 0.8 mm/s, and the optimized specimen bending strength was 103.1 ± 5.24 MPa. The deposited line with a flat section shape and width greater than the print spacing helped to reduce the porosity of the specimens. The process parameters that resulted in large high-temperature areas and a high extrusion pressure could better promote material fusion.

Keywords: Additive manufacturing; Composite material; Biodegradable bone plate; Orthogonal experiment; Bending strength

*Correspondence to: Wurikaixi Aiyiti, School of Mechanical Engineering, Xinjiang University, Urumqi 830000, PR China; wurikaixi@xju.edu.cn

Received: November 8, 2021; **Accepted:** November 30, 2021; **Published Online:** December 17, 2021

Citation: Aihemaiti P, Jiang H, Aiyiti W, *et al.*, 2022, Optimization of 3D Printing Parameters of Biodegradable Polylactic Acid/Hydroxyapatite Composite Bone Plates. *Int J Bioprint,* 8(1):490. http:// doi.org/10.18063/ijb.v8i1.490

1. Introduction

Additive manufacturing (AM), also known as three-dimensional (3D) printing or rapid prototyping, has been widely applied in various fields, including manufacturing, medicine, architecture, and art[1]. The combination of AM with digital medical imaging technology, reverse engineering, and computer-aided design (CAD) can provide support for the accurate and customized treatment of patients based on their individual characteristics[2]. The application of AM in orthopedics is the main use of AM in the medical field and customized implants are one of the key applications of 3D printing in orthopedics[3]. Orthopedic implants include trauma implants (e.g., plates and screws)[4,5], spinal implants (such as artificial vertebral bodies and cages)[6], joint implants (e.g., artificial hip joints and knee joints)[7,8], personalized prostheses (e.g., scapular prosthesis, chest prostheses, and rib prostheses)[9-11], and bone tissue engineering scaffolds[12-14].

Metal implant materials have excellent mechanical properties, but its elastic modulus is much higher than that of human bone and will lead to stress shielding[15]. Unlike artificial joints, cages, and other implants that do not need to be removed after implantation into the human body, metal plates need to be removed after fracture healing to avoid stress shielding[16]. The ideal plate should realize strong fixation in the early stage of fracture treatment and prevent osteoporosis of the fixed bone induced by stress shielding in the later stage. If the plate is degradable, it can degrade and crack gradually with fracture healing, and the stress shielding effect will gradually decrease until it disappears completely, which is conducive to the conduction of physiological stress and accelerates the formation and reconstruction of bone. At the same time, it does not need to be removed again through surgery[17,18].

Polylactic acid (PLA) is a kind of promising polymer for use in various biomedical applications owing to its

high biocompatibility and biodegradability. It is often used to make degradable scaffolds, bone plates, and other implants. The bone plates are different from long-term orthopedic implants such as artificial joints and cages, some non-degradable bone plates need to be removed after the fracture is healed, which will make the patients undergo another operation. Degradable bone plates do not need to be removed after fracture healing, but common degradable materials, such as PLA, have poor mechanical properties, and the acid products produced by degradation process can easily lead to aseptic inflammation[19,20]. The strength of a composite composed of bioceramic particles as the reinforcing phase in PLA is higher than that of pure PLA. Hydroxyapatite (HA) is a widely used biodegradable bioceramic. The addition of HA can not only improve the bone integration ability and biocompatibility of implants, but also produce a slightly alkaline environment in the degradation process, which helps to reduce the occurrence of aseptic inflammation. Huang *et al*. grafted poly (D-lactide) (PDLA) oligomers onto HA nanorods (HA-PDLA), and the HA-PDLA hybrids were mixed with poly (L-lactide acid) (PLLA) to improve the tensile strength and the elongation[21]. Shikinami *et al*. investigated the forged composites of raw HA particles and PLLA (PLLA/F-u-HA) bone rods that exhibited bioactivity and biodegradation[22]. The strength stability, bioactivity, and biodegradation properties were ideal for bone repair. Takayama *et al*. studied the effects of a bimodal distribution of micro-HA and nano-HA (nHAP) particles on the mechanical properties, such as the bending strengths, modulus, and mode *I* fracture energies of PLLA/HA composites[23]. The bending properties and fracture energies were effectively improved using a bimodal distribution instead of a monomodal distribution. Nejati *et al*. prepared nHAP/PLLA composite scaffolds with porosities of 85%[24]. Experimental results showed that the cell affinity and compatibility of the material were superior to those of pure PLLA and PLLA micro composites.

PLA and bioceramic particles were mixed in different proportions to make different composite filaments, which could be conveniently used to make a composite model by a fused deposition modeling (FDM) printer. In the FDM printing process, minimizing the voids and improving the adhesion between deposited lines are the keys and challenges for improving the printing quality[25,26]. The process parameters are among the main factors affecting the mechanical properties of FDM printed parts[27-29]. There are relatively many studies on the relationship between the process parameters and mechanical properties of printed parts[30-34], but there are few studies on the formation mechanism of the internal microscopic defects of printed parts and their influence on the mechanical properties of the parts.

In this study, a PLA/HA composite plate was proposed. The important process parameters involved in bone plate printing, such as the HA content, layer thickness, printing speed, and filament feeding speed, were optimized by an orthogonal experiment. Combined with the analysis of the internal defects, the temperature of the printing process, and the printing pressure, the influence of the process parameters on the bending strengths of the bending specimens were studied.

2. Materials and methods

According to the stress characteristics of the plate, the influence of the process parameters on the bending mechanical properties of the plate was analyzed. To simplify the analysis process, the influence of the screw holes in the plate samples was not considered.

2.1. Materials

PLA filament and two kinds of PLA composite filaments with different HA contents (HA mass ratios in 10% and 20%) were used to prepare samples for bending experiments. The average size of HA particles is 15 μm. The diameter of the filaments is 1.75mm, which were supplied by Shaanxi Jugao AM medical corporation.

2.2. Experimental setup

(1) Printing platform

The 3D printer used in this study is shown in **Figure 1A**. It consisted of a three-axis closed-loop servo motion system, a hotbed, a nozzle, and a temperature control system. The hotbed was the substrate for the molten filament deposition, which was installed on the worktable that was controlled by the motion control system for X-Y

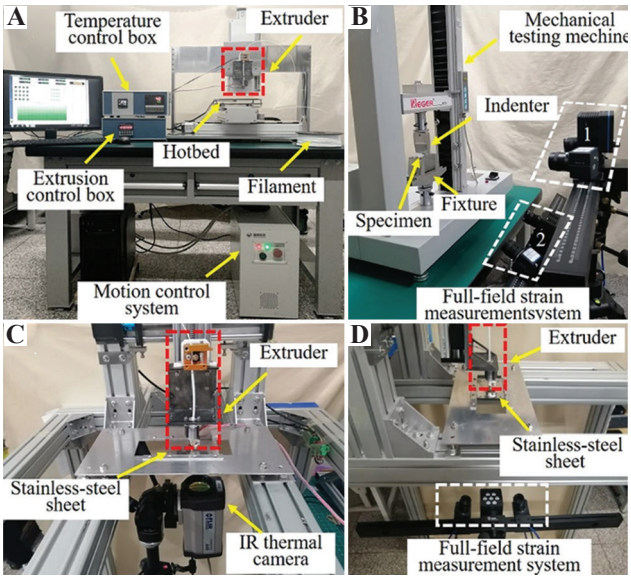

Figure 1. (A) 3D printing platform. (B) Mechanical test machine and 3D full-field strain measurement setup. (C) Printing temperature measurement setup. (D) Printing pressure measurement setup.

plane motion. The extruder was installed on the Z-axis worktable. After slicing the 3D CAD model and setting the scanning mode, a G-code file containing the printing path was generated and imported into the motion control software of the 3D printer to start the printing.

(2) Mechanical test and 3D full-field strain measurement setup

A mechanical testing machine (3005t, Shenzhen Regel Instrument Co., Ltd., China) was used for three-point bending experiments. During the bending experiments, a 3D full-field strain measurement system (3DFSMS) (XTOP 3D Technology (Shenzhen) Co., Ltd.) was applied to photograph and analyze the deformation and 3D strains of the specimens, as shown in **Figure 1B**. The system contained two camera groups, each with a pair of cameras. The camera groups could cooperate with each other to detect and analyze a sample from different directions simultaneously. Camera group 1 captured the front surface of the specimen, and camera group 2 captured the lower surface of the bending specimen. The surfaces of all the specimens were initially painted with white paint as a background, after which they were covered with a random black paint speckle pattern.

(3) Printing temperature measurement setup

The printing temperature of a single deposited line was measured and analyzed by an infrared thermal camera (FRIL A40). The experiment setup is shown in **Figure 1C**. Single lines were deposited in the thin stainless-steel sheet (0.08 mm). When the nozzle deposited a line in the stainless-steel sheet, the infrared thermal camera captured the dynamic variation process of the temperature field on the bottom surface of the sheet during the printing process.

(4) Printing pressure measurement setup

To compare the printing pressures of different process parameters, 3DFSMS was used to measure the deformation of stainless-steel sheets (0.08 mm) during the single-line deposition. The experimental setup is similar to the temperature measurement setup shown in **Figure 1D**.

2.3. Experiment methods

(1) Orthogonal experimental design

Four important process parameters, including the HA content (mass ratio), layer thickness, printing speed, and filament feeding speed, were studied by an orthogonal experiment. Orthogonal experiments L9 with four factors and three levels were designed according to our former research, as shown in **Table 1.** The nozzle diameter of 0.4 mm, printing temperature of 210°C, hotbed temperature of 40°C, and printing spacing of 0.4 mm were set as the constant parameters in the experiments.

(2) Bending experiment

The cuboid specimens were designed according to the ISO 178-2018 test standard, and the specimen dimensions are 80 mm × 10 mm × 4 mm. Bending specimens of nine schemes according to the orthogonal experiment were fabricated by the 3D printing platform as described in **Figure 1A**. Five specimens were printed for each group of process parameters.

The mechanical test and 3DFSM of the specimen were performed in the experimental setup shown in **Figure 1B**. According to the requirements of the test standard, the span of the bending specimens was 64 mm, and the loading rate was 2 mm/min. The load and displacement values of the tested specimen were recorded, and the bending stress and strain were calculated according to the obtained load and displacement after the bending experiments.

(3) Internal defect analysis of specimen

The existence of pore defects in FDM printed parts is a common problem. Therefore, different failure forms of the specimens should be related to the internal defects. A micro-X-ray 3D imaging system (YXLON Cheetah, Germany) was used to detect and reconstruct the internal defects of the specimens, and the internal pore geometries, volumes, and spatial distributions were also analyzed. **Figure 2A** shows the diagram of the sampling area for the defect analysis obtained using the micro-X-ray 3D imaging system. The scanning range was 10 mm × 7 mm × 3 mm. A scan resolution of 15 μm, a peak tube potential of 80 kV, and a target current of 62.5 μA were set as the basic measurement parameters.

(4) Analysis of cross-sectional geometry of the single deposited line

In FDM printing, the molten material is extruded from the nozzle, and a line is deposited on the hotbed (or the front

Table 1. Factors and their levels

Factors	HA content A (%)	Layer thickness B (mm)	Printing speed C (mm/s)	Filament feeding speed D (mm/s)
Level 1	0	0.1	30	0.7
Level 2	10	0.15	40	0.8
Level 3	20	0.2	50	0.9

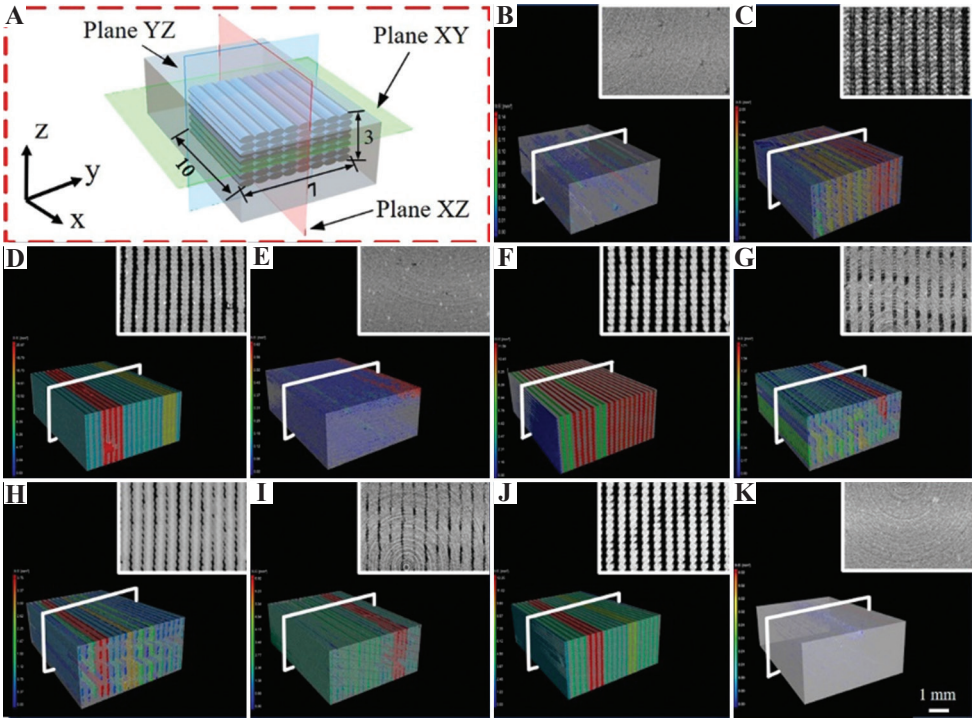

Figure 2. (A) Schematic of the sampling area for defect analysis. (B-K) Internal defect analysis of specimens of schemes 1-10.

layer). Another line is then deposited next to the front deposited line at a certain distance so that the printed plane is completed by reciprocating. In this study, the same print spacing (i.e., the center distance of two adjacent deposited lines) for all specimens was 0.4 mm. Therefore, there should be a close relationship between the internal defect form, porosity, and section shape of the deposited line.

For the nine schemes of the orthogonal experiment and the optimized scheme, single deposited lines were printed. After cutting in the middle of the deposited line, the geometry, width, and height of the cross-section were observed and measured by a digital microscope (VHX-6000, KEYENCE, Japan).

(5) Overlap rate calculation

The overlap rate is a significant parameter. The diagram of the overlap is shown in **Figure 3**, the width of the deposited line is W, the height of the deposited line is H, and the print spacing between two adjacent lines is C. The overlap rate can be calculated as follows:

$$R = \frac{S3}{S1} \cdot 100\% \quad (1)$$

In Eq. 1, *S3* is the overlapping area of the two adjacent deposited lines, and *S1* and *S2* are the cross-sectional areas of two adjacent lines. A larger overlap rate means that the overlapping area between two adjacent deposited lines is larger.

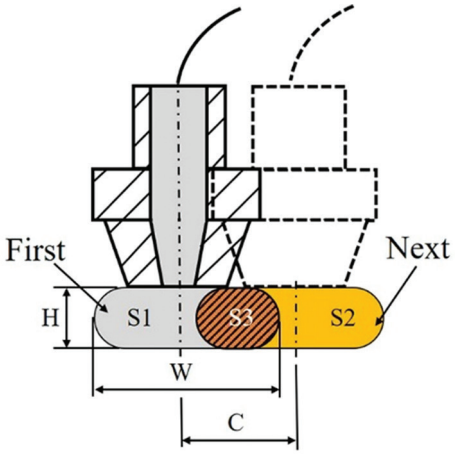

Figure 3. Schematic of the overlapping model.

(6) Print temperature measurement

The printing temperature is a key parameter in the FDM process. The fusion of two adjacent deposited lines and adjoining layers depends on the hot molten material extruded from the nozzle melting the neighboring solidified material. The high temperature of the molten material extruded from the nozzle makes it easier to bond firmly with the neighboring materials by fully melting the surrounding solidified material. In contrast, this will lead to an insufficient bonding strength between lines and between layers, causing the specimen to easily fail under the influence of external forces[35,36].

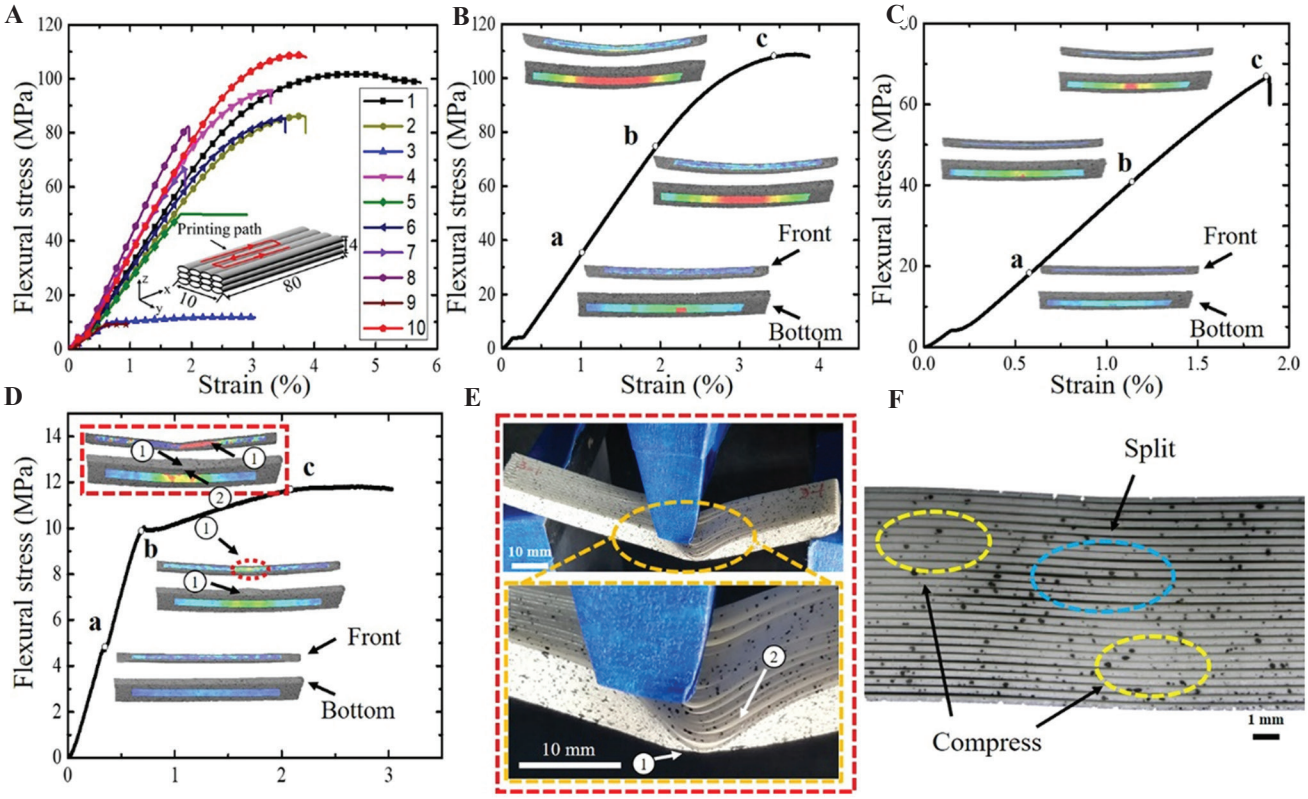

Figure 4. (A)Stress-strain curves of bending tests. (B-D) Flexural curve and 3DFSM images of scheme 10, scheme 8, and scheme 3. (E) Distorted specimens. (F) Failure of the specimen surface.

The printing temperature of a single deposited line was measured and analyzed by the experimental setup shown in **Figure 1C**. The sampling frequency of the infrared thermal camera was set as 50 Hz, and the focus distance was set as approximately 70 mm from the bottom surface below the stainless-steel sheet.

(7) Printing pressure measurement

The material fusion of the FDM process relies on the temperature of the extruded molten filament that heats the material in the surrounding solidified state to bond it together. If there is adequate pressure between the melted filament and the surrounding solidified material, it could help the bonding effect between the materials.

The stainless-steel sheet was roughed with sandpaper (1800 mesh) to avoid surface reflection. Then, 75% alcohol was used to clean the surface to remove the residue from the stainless-steel sheet. After roughing, the sheet was spray-painted, first with white paint as the background color and then with black as scattered spots. The sheet was fixed on the platform, and the painted surface was faced down to the 3DFSMS. The deformation of the sheet was dynamically measured when a single deposited line was printed on the upper surface of the sheet. During the experiment, to avoid pressure fluctuations when starting the filament extrusion, the initial position of the nozzle was outside the sheet. The filament then began extrusion, and when the feeding process was stable, the nozzle began to move toward the thin plate and began to collect deformation data. The capture frequency of the camera was set to 5 ms, and the focus distance was set to 530 mm.

(8) Fracture analysis of specimens

To analyze the bending fracture characteristics of specimens made of three kinds of filaments, the cross-sectional morphologies of the three specimens with different HA contents were observed using field-emission electron scanning microscopy (FESEM, JSM-7610Plus, Japan). The three filaments were a PLA filament, a PLA/HA (10%) composite filament, and a PLA/HA (20%) composite filament.

3. Results and discussion

3.1. Analysis of bending experiment results

Figure 4A shows the bending stress-strain curves of the nine groups of specimens in the orthogonal experiment. **Table 2** shows the bending strengths of nine groups of specimens in the orthogonal experiment.

The effects of the printing parameters on the mechanical properties were studied through the analysis of variance (ANOVA). **Table 3** shows the variance analysis

Table 2. Parameters and results of orthogonal experiment

Scheme No.	HA content A (%)	Layer thickness B (mm)	Printing speed C (mm/s)	Filament feeding speed D (mm/s)	Bending strength (MPa)
1	0	0.1	30	0.7	97.2±7.85
2	0	0.15	40	0.8	82.1±4.81
3	0	0.2	50	0.9	11.7±0.35
4	10	0.1	40	0.9	96.2±4.58
5	10	0.15	50	0.7	30.9±12.86
6	10	0.2	30	0.8	80.4±8.08
7	20	0.1	50	0.8	63.5±3.65
8	20	0.15	30	0.9	71.7±13.70
9	20	0.2	40	0.7	10.6±2.16

Table 3. Range and variance analysis (ANOVA) for bending strength

Type of data processing	HA content A (%)	Layer thickness B (mm)	Printing speed C (mm/s)	Filament feeding speed D (mm/s)
Range analysis				
T1	63.7	85.6	83.1	46.4
T2	69.2	61.6	63.1	75.3
T3	48.7	34.4	35.4	59.9
R	20.45	51.25	47.75	28.95
Sequence			B>C > D>A	
Optimal levels	A2	B1	C1	D2
Optimal combination			A2B1C1D2	
Variance analysis				
SS	2687.82	15779.22	13797.42	5036.22
DF			2	
MS	1343.91	7889.61	6898.71	2518.11
F	22.309	130.97	114.52	41.801
P	0.000002	1.2663×10^{-14}	6.4749×10^{-14}	5.4023×10^{-9}

results for the bending strength. The layer thickness was the most important factor in determining the bending strength of the 3D-printed specimens, followed by the printing speed, filament feeding speed, and HA content.

According to the main effect parameters of each factor shown in **Table 3**, the best combination of process parameters was A2B1C1D2, that is, the bending strength was maximized when the HA content was 10%, the layer thickness was 0.1 mm, the printing speed was 30 mm/s, and the filament feeding speed was 0.8 mm/s.

The optimized parameters are not found in the nine schemes of the orthogonal experiment. Therefore, the optimized parameters were used for supplementary experiments, and specimens were prepared for verification experiments. The average bending strength of the specimens was 103.1 ± 5.24 MPa, which was better than those of the nine schemes in **Table 2**. Scheme 10 was used to represent the optimized parameter combination obtained by the orthogonal experiment.

Figure 4B shows the bending curve of scheme 10, and the strain images obtained from 3DFSM of the front and bottom surfaces corresponded to three points, a, b, and c, on the curve. The strain image coincides with the trends of the bending experimental curves. With loading, the bending deformation process of the specimen was relatively smooth. Starting from point b, the specimen entered a distinct plastic deformation stage, and the bending displacement increased gradually until it broke. The specimen showed good mechanical properties during the loading process.

Figure 4C shows the bending curve and the 3DFSM images of scheme 8. The curve shows that the bending specimen broke without noticeable plastic deformation. The 3DFSM images show that there was a significant stress concentration at point c. The failure mode of scheme 7 was similar to that of scheme 8.

The stress-strain curve of scheme 3 (**Figure 4D**) shows that stage a-b was basically elastic deformation. Point b is the inflection point, and the curve varies gently after point b. **Figure 4E** shows the state of the specimen at point c. The specimen surface had significant distortion and depression. There was no red area symmetric to the

specimen center in the 3DFSM image. The red area in the front image is on the right side of the sample, which corresponds to the distorted and collapsed part shown in the photograph on the right side of **Figure 4E**, indicating that the stress concentration here was significant. In the bottom image, there were several scattered red areas instead of continuous red areas in the middle area. As shown in the photograph on the right in **Figure 4F**, the distortion deformation led to the dislocation of parallel deposited lines, tearing in some areas, and uneven stress distribution on the bottom. When the indenter was raised, the distortion of the specimen largely recovered, but curved and cracked deposited lines were still visible. The failure modes of schemes 5 and 9 were similar to that of scheme 3.

3.2. Internal defect analysis of specimen

Figure 2 shows the scanned and reconstructed images of the specimens. The colored areas in the figure represent pores, and the volumes of the pores are represented by different color ranges. The porosity and corresponding bending strength of each specimen are shown in **Table 4**. The porosity of the specimen affects its bending strength. The specimens with higher bending strength have small porosity. The porosity of scheme 3 was the highest, reaching 49.71%, and the corresponding bending strength was 11.7 ± 0.35 MPa. The porosity of the specimen with optimized parameters (scheme 10) was 0.18%, and the bending strength was 103.1 ± 5.24 MPa.

The porosities of the specimens built in schemes 3, 9, and 5 ranked in the top three of all the schemes. The 3D reconstruction model of the internal defects of the specimens showed that the interiors of the specimens were composed of several unconnected thin-walled walls, and gaps between the thin walls were evident. The stability of the thin-walled wall structure was poor, and it was easily destabilized under the bending loads. Thus, the specimen distorted and collapsed as shown in **Figure 4E**.

Table 4. Porosity analysis results and flexural strengths of specimens

Scheme	Porosity (%)	Flexural strength (MPa)
1	0.62	97.2±7.85
2	10.37	82.1±4.81
3	49.71	11.7±0.35
4	3.08	96.2±4.58
5	35.35	30.9±12.86
6	11.37	80.4±8.08
7	12.44	63.5±3.65
8	11.76	71.7±13.70
9	45.9	10.6±2.16
10	0.18	103.1±5.24

3.3. Analysis of cross-sectional geometry of the single deposited line

Figure 5 shows the geometry, width, and height of the cross-section of the single deposited line which was observed and measured by the digital microscope. The cross-sectional shapes and sizes of the deposited lines were significantly different. The cross-sectional shapes of the deposited lines were mostly flat. For schemes 1 and 10, the widths of the deposited lines were slightly larger than the diameters of the bottom surface of the nozzle. The width of other deposited lines did not exceed the diameter of the bottom surface (0.65 mm), and its height was equivalent to the set layer thickness. This showed that the nozzle bottom surface had the function of flattening and spreading the molten filament from the nozzle hole. When the width of the deposited line was <0.4 mm, there was no contact between adjacent deposited lines. The widths of the deposited lines in schemes 3, 5, and 9 were less than the print spacing; hence, the deposited lines did not overlap in the horizontal direction. As a result, several unconnected thin walls formed.

Figure 6 shows the relationships between overlap rate, porosity and bending strength for all the schemes. As shown, the schemes with high bending strength have smaller porosity and larger overlap rate.

3.4. Analysis of printing temperature

Figure 7 shows the top view appearance and temperature contours of a single line, which was printed by ten schemes. Based on the data shown in **Table 2,** some orthogonal experiment schemes with relatively good bending strengths had larger high-temperature areas during the printing process, and the shapes of the high-temperature areas were uniform and showed comet-like appearances. The top view of the corresponding deposited line shows that the width of the deposited line was larger and had a uniform shape. The large width of the deposited line indicated that the extrusion of material per unit time was greater. The cooling speed was relatively low, which was more conducive to full integration with the surrounding material. In contrast, schemes with poor bending strengths had small areas of high-temperature field during the printing process, and the shapes of the high-temperature areas were irregular. For example, the temperature field image of scheme 5 showed that the overall temperature was low and varied with a wavy shape, and the shape of the corresponding deposited line also showed a wide and narrow uneven shape. The irregular width of the deposited line could lead to insufficient binding and gap formation. Low temperatures affected the bonding quality between adjacent lines when overlapping.

The temperature of the extruded material at the nozzle outlet and in contact with the substrate was measured from the side using an infrared thermal camera and the results are shown in **Table 5**. In general, the outlet temperatures of

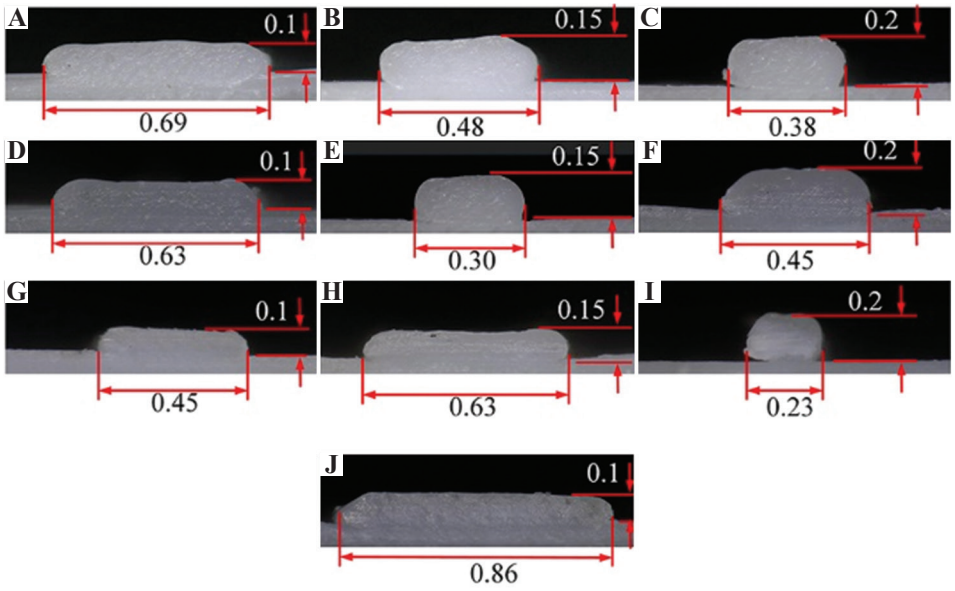

Figure 5. (A-J) Cross-sectional shapes of single deposited line of scheme 1-10.

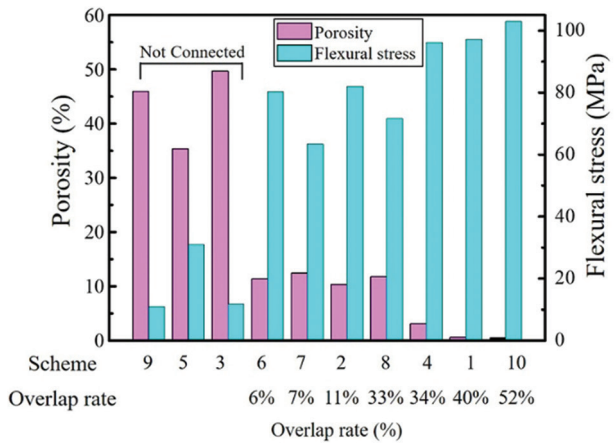

Figure 6. Effect of overlap rate on porosity and flexural strength.

Table 5. Temperature measurement results of outlet/substrate

Scheme	Outlet temperature (°C)	Substrate temperature (°C)	Temperature gap (°C)
1	191.6	174.6	17.1
2	167.0	152.8	14.2
3	178.2	174.0	4.2
4	201.2	160.9	40.3
5	190.2	170.8	19.4
6	188.8	159.8	29.0
7	212.6	154.3	58.3
8	202.4	161.8	40.6
9	196.6	146.2	50.4
10	207.9	169.3	38.6

the experimental group of PLA/HA filaments were higher than those of the PLA filament, and the temperature of the 20% HA filament was higher. The temperature of the molten material in the nozzle outlet had little to do with the printing speed, the layer thickness, or the filament feeding speed. It mainly depended on the temperature of the nozzle and the properties of the material. With the same heating temperature as the nozzle, the HA content increased, making it easier for the material to be heated to a higher temperature. After the material was extruded from the nozzle, the temperature-drop status of different schemes varied, and the temperature drop of the 20% HA filament was significantly greater than that of the other two materials due to a number of factors.

When the extruded material reached the substrate (or front layer), a larger high-temperature area of the molten material was conducive to the full fusion of the extruded material with the surrounding material. The melting point of PLA is 150 – 180°C. The comparison of the optimized scheme 10 with scheme 9 shows that the temperature on the substrate for scheme 10 reached the melting point range of the PLA. However, the temperature of the molten material of scheme 9 on the substrate was lower than the melting point of PLA. Furthermore, the width of the deposited line printed in the optimized scheme 10 was 3.7 times that of scheme 9, which could melt and fuse a larger area of solidified materials. The temperature of the deposited line printed in scheme 3 on the substrate was the highest among all the parameters, mainly because the high filament feeding speed led to more materials being extruded onto the substrate per unit time, resulting in a slow cooling speed within the distance from the nozzle to the substrate. However, because the layer thickness

of scheme 3 was 0.2 mm and the printing speed was 50 mm/s, the deposited line was narrow and high, the high-temperature area was small (as shown in **Figure 7),** and the width was less than the print spacing. Thus, the adjacent materials could not be fully integrated, resulting in cracks along the height direction.

3.5. Analysis of printing pressure

Figure 8A shows the deformation contour of the sheet under the pressure of the extruded materials, which was captured by the 3DFSMS as detailed in **Figure 1D**. To compare the deformation differences of each scheme directly, a section line was drawn perpendicular to the movement direction of the nozzle. The displacement data on the section line were extracted for analysis. The process parameter with the maximum deformation of the sheets showed a high bending strength.

Figure 8 illustrates the pressure generation mechanism and sheet deformation when printing with different process parameters. The color cloud diagram shows the deformation of the sheet captured by the 3DFSMS. The curve was a deformation curve corresponding to each scheme. The deposited line with a flat cross-section extended to both sides of the nozzle under the constraints of the surface around the nozzle outlet. Under the pressure of the filament extrusion, the molten material was squeezed into the previously deposited lines. The moving nozzle, which acted like an iron, was used to iron the molten filament. Therefore, the pressure that caused the deformation of the sheet included the pressure of the filament extrusion and the pressure of the flowing melted material, which is called the printing pressure in this paper. A larger cross-sectional width of the deposited line correlates with a greater deformation of the thin plate, indicating a greater printing pressure. According to the width measurement of a single line printed in each scheme in **Figure 5**, the cross-sectional widths of schemes 3, 5, and 9 were less than the outlet diameter (0.4 mm) of the nozzle, indicating that the extruded material fell on the sheet and was stretched before solidifying. The sheet underwent only a relatively small deformation under the pressure of the filament extrusion.

In summary, the porosity was a key factor affecting the flexural strength. The cross-sectional geometries of the deposited lines printed by different process parameters were different, which led to different porosities. To be specific, the relationship between the widths of the deposited lines and the center distance of two adjacent deposited lines affected the specimen porosity. When the width of the deposited line was less than the print spacing between two adjacent deposited lines, a gap was created between the two lines, and several parallel thin wall structures were formed that were not connected after multiple-layer stacking. Under the applied bending load, the thin-walled structure was unstable, resulting in distortion and collapse of the specimen. When the cross-sectional width was greater than the print spacing, the two adjacent deposited lines could be fully fused, and when the cross-sectional width became larger, the porosity of the specimen became smaller. The printing temperature and pressure were important factors for ensuring the full integration between deposited lines. A higher temperature of the deposited lines was more conducive to melting the surrounding solidified materials. A higher printing pressure was more conducive to combining the melted materials.

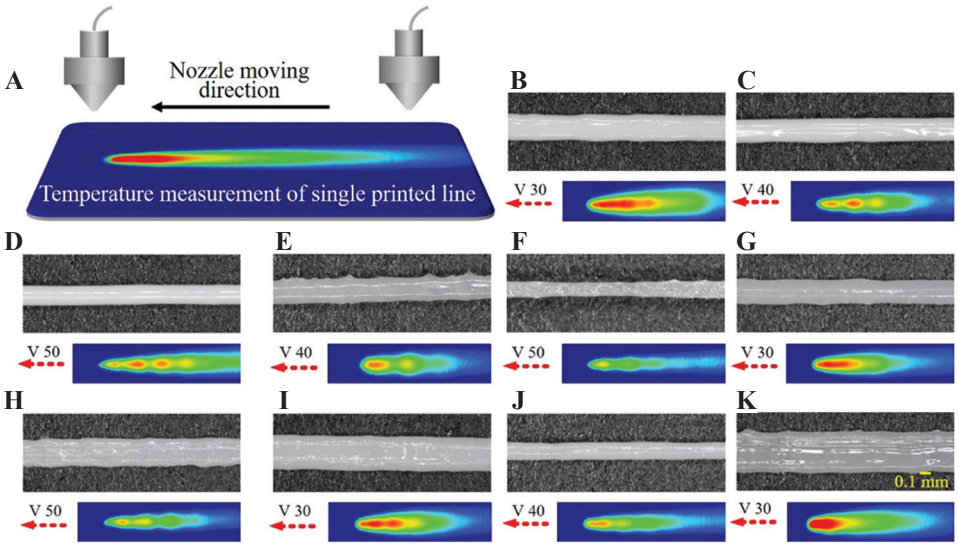

Figure 7. (A) Schematic of temperature measurement on the bottom surface of the sheet. (B-K) Temperature measurement results and top view appearance of the single deposited line of schemes 1-10.

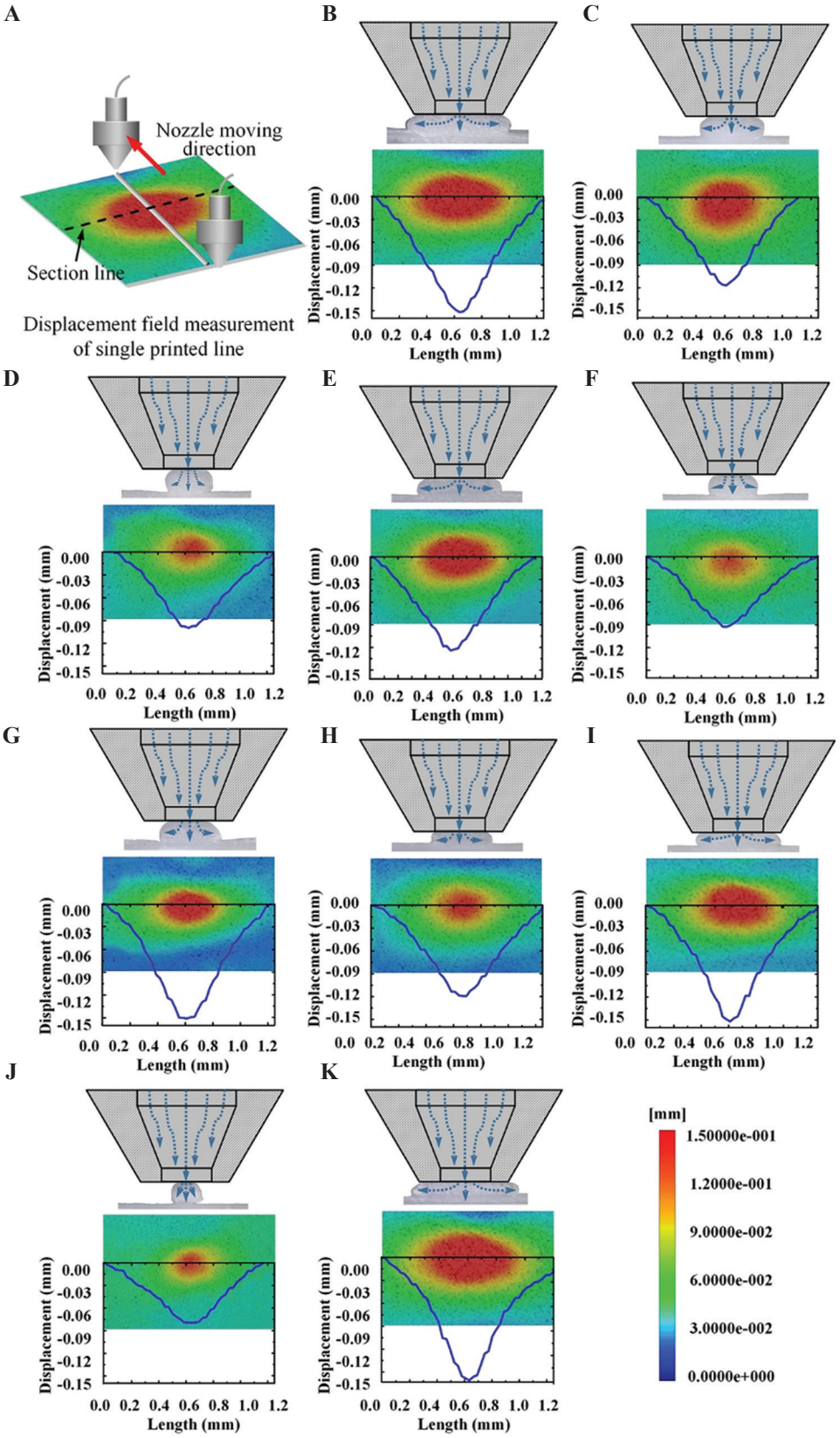

Figure 8. (A) Schematic of the printing pressure analysis. (B-K) Diagram of the extruding process, the cross-sectional geometry of a single deposited line, and printing pressure images and curves of schemes 1-10.

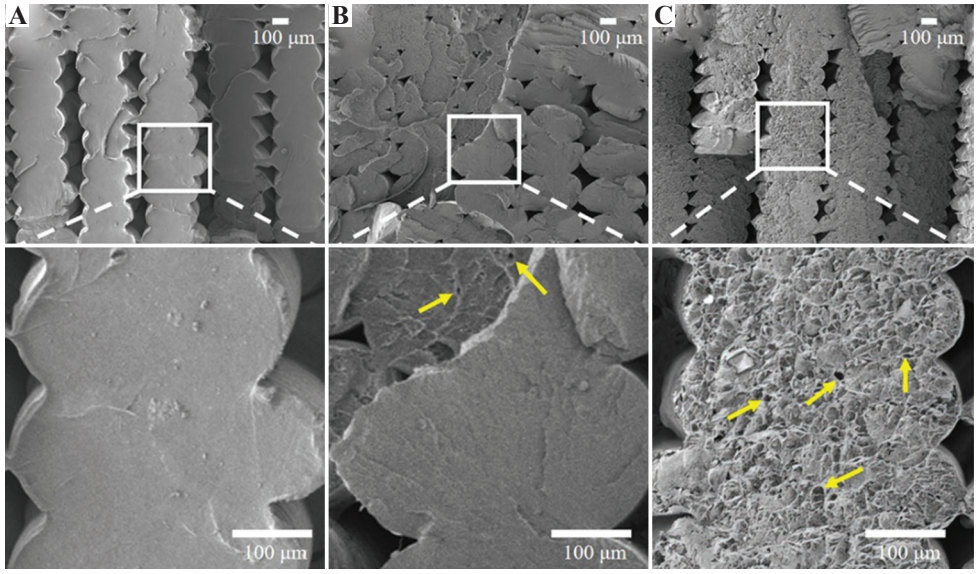

Figure 9. Morphologies of the specimens' fracture surfaces. (A) Scheme 2. (B) Scheme 6. (C) Scheme 7.

Without considering the HA content, it seems that when the layer thickness was thinner, the printing speed was lower, and the filament feeding speed became faster. As a result, it was easier to achieve high printing pressures, high temperatures of the material during extrusion, and the introduction of more materials, resulting in deposited lines with larger cross-sectional widths. However, when the layer thickness is smaller, printing speed is slower, and the filament feeding speed is faster, it will increase filament feeding resistance. This would cause nozzle blockages and filament feeder gear slipping. The specimen prepared with the optimal scheme 10 showed a large cross-section width, high printing temperature, and high printing pressure. Finally, the specimen with a porosity of 0.18% and a bending strength of 103.1±5.24 MPa was prepared.

3.6. Fracture analysis results of specimens

Based on the results with the optimized parameters, a higher HA content does not yield a better bending performance. The cross-sectional morphologies of three specimens with different HA contents were also different. **Figure 9A** shows the cross-sectional morphology of scheme 2 (pure PLA), **Figure 9B** shows scheme 6 (PLA/HA [10%]), and **Figure 9C** shows scheme 7 (PLA/HA [20%]).

The section surface of the PLA specimen was relatively smooth, and the section surface of the PLA/HA (10%) specimen was slightly rough. The section surface of the PLA/HA (20%) specimen was very rough, and a large number of dimples and pores in the deposited line were evident. An excessive HA content could lead to an increase in the micro-porous defects inside the specimen, which may have been caused by the air around the HA particles expanding during heating to produce tiny bubbles, thereby reducing the mechanics of the specimen.

4. Conclusions

The process parameters for the 3D printing of PLA/HA composite plates were optimized in an orthogonal experiment. The effects of the layer thickness, printing speed, filament feeding speed, and HA content on the bending strengths of the specimens were analyzed. The main conclusions are as follows:

- The factors affecting the bending properties of PLA/HA specimens were the layer thickness, printing speed, filament feeding speed, and HA content, successively. The optimized specimen's bending strength was 103.1 ± 5.24 MPa.
- The internal defects of the specimen had a significant effect on the bending strengths of the specimens. Specimens with large porosities exhibited low bending strengths. Scheme 3 had a porosity of 49.71%, and the bending strength was only 11.7 ± 0.35 MPa. The specimen printed with the optimized parameters had a porosity of 0.18% and a maximum bending strength.
- When the print spacing was consistent, the cross-sectional size of a single deposited line had a significant effect on the specimen porosity. Deposited lines with flat section shapes and widths greater than the print spacing helped reduce the porosity of the specimen. The schemes with high bending strength have smaller porosity and larger overlap rate.

- When the process parameters yielded larger areas of high temperature, the specimen had good mechanical properties. Larger areas could be heated, and the heat dissipation was relatively slow for those parameters, making it easier to fully bond with the surrounding materials.
- A high printing pressure of the material during printing helped the material spread to both sides, filling the gap between two adjacent lines and reducing the porosity. A high pressure of the molten material helped to improve the bonding quality between adjacent deposited lines and layers.
- When the HA content was 20%, the cross-section was rough compared to those of the pure PLA and 10% HA specimens. Furthermore, it contained a large number of dimples and pores, thus reducing the bending properties of the specimen.

Acknowledgments

We would like to acknowledge the financial support of the Natural Science Foundation of Xinjiang Uygur Autonomous Region of China (No. 2019D01C040) and the Postgraduate scientific research innovation project of Xinjiang Uygur Autonomous Region of China (No. XJ2021G047).

Conflict of interest

The authors reported no potential conflict of interest in this study.

Author contributions

P.A. designed and performed the experiments, data analysis, and drafted the manuscript. H.J. participated in and assisted in most experiments. W.A. supervised the entire research process. A.K. assisted in internal defect testing.

References

1. Ngo TD, Kashani A, Imbalzano G, *et al.*, 2018, Additive Manufacturing (3D Printing): A Review of Materials, Methods, Applications and Challenges. *Compos B Eng*, 143:172–96. https://doi.org/10.1016/j.compositesb.2018.02.012
2. Bozkurt Y, Karayel E, 2021, 3D Printing Technology; Methods, Biomedical Applications, Future Opportunities and Trends. *J Mater Res Technol*, 14:1430–50. https://doi.org/10.1016/j.jmrt.2021.07.050
3. Kumar R, Kumar M, Chohan JS, 2021, The Role of Additive Manufacturing for Biomedical Applications: A Critical Review. *J Manuf Processes*, 64:828–50. https://doi.org/10.1016/j.jmapro.2021.02.022
4. Dos Santos T, Merlini C, Aragones A, *et al.*, 2019, Manufacturing and Characterization of Plates for Fracture Fixation of Bone with Biocomposites of Poly (Lactic Acid-Co-Glycolic Acid) (PLGA) with Calcium Phosphates Bioceramics. *Mater Sci Eng C Mater Biol Appl*, 103:109728. https://doi.org/10.1016/j.msec.2019.05.013
5. Dhandapani R, Krishnan PD, Zennifer A, *et al.*, 2020, Additive Manufacturing of Biodegradable Porous Orthopaedic Screw. *Bioact Mater*, 5:458–67. https://doi.org/10.1016/j.bioactmat.2020.03.009
6. Tong Y, Kaplan DJ, Spivak JM, *et al.*, 2020, Three-Dimensional Printing in Spine Surgery: A Review of Current Applications. *Spine J*, 20:833–46. https://doi.org/10.1016/j.spinee.2019.11.004
7. Xia RZ, Zhai ZJ, Chang YY, *et al.*, 2019, Clinical Applications of 3-Dimensional Printing Technology in Hip Joint. *Orthop Surg*, 11:533–44. https://doi.org/10.1111/os.12468
8. Wang F, Chen H, Yang P, *et al.*, 2019, Three-Dimensional Printed Porous Tantalum Prosthesis for Treating Inflammation after Total Knee Arthroplasty in One-Stage Surgery-a Case Report. *J Int Med Res*, 48:1-10. https://doi.org/10.1177/0300060519891280
9. Xiao R, Feng X, Fan R, *et al.*, 2020, 3D Printing of Titanium-Coated Gradient Composite Lattices for Lightweight Mandibular Prosthesis. *Compos B Eng*, 193:108057. https://doi.org/10.1016/j.compositesb.2020.108057
10. Liu D, Fu J, Fan H, *et al.*, 2018, Application of 3D-Printed PEEK Scapula Prosthesis in the Treatment of Scapular Benign Fibrous Histiocytoma: A Case Report. *J Bone Oncol*, 12:78–82. https://doi.org/10.1016/j.jbo.2018.07.012
11. Zhang C, Wang L, Kang J, *et al.*, 2020, Bionic Design and Verification of 3D Printed PEEK Costal Cartilage Prosthesis. *J Mech Behav Biomed Mater*, 103:103561. https://doi.org/10.1016/j.jmbbm.2019.103561
12. Hedayati SK, Behravesh AH, Hasannia S, *et al.*, 2020, 3D Printed PCL Scaffold Reinforced with Continuous Biodegradable Fiber Yarn: A Study on Mechanical and Cell Viability properties. *Polym Test*, 83:106347. https://doi.org/10.1016/j.polymertesting.2020.106347
13. Wang W, Zhang B, Li M, *et al.*, 2021, 3D Printing of PLA/n-HA Composite Scaffolds with Customized Mechanical Properties and Biological Functions for Bone Tissue Engineering. *Compos B Eng*, 224:109192.

https://doi.org/10.1016/j.compositesb.2021.109192

14. Yang Y, Wang G, Liang H, *et al.*, 2019, Additive Manufacturing of Bone Scaffolds. *Int J Bioprint*, 5:148. https://doi.org/10.18063/IJB.v5i1.148
15. Rony L, Lancigu R, Hubert L, 2018, Intraosseous Metal Implants in Orthopedics: A Review. *Morphologie*, 102:231–42. https://doi.org/10.1016/j.morpho.2018.09.003
16. Gupta SK, Shahidsha N, Bahl S, *et al.*, 2021, Enhanced Biomechanical Performance of Additively Manufactured Ti-6Al-4V Bone Plates. *J Mech Behav Biomed Mater*, 119:104552. https://doi.org/10.1016/j.jmbbm.2021.104552
17. Jung GS, Kwon JH, Lee JW, *et al.*, 2017, A New Approach to Nasomaxillary Complex Type of Nasal Bone Fracture: Clip Operation. *J Craniomaxillofac Surg*, 45:954–61. https://doi.org/10.1016/j.jcms.2017.03.020
18. Ueki K, Moroi A, Yoshizawa K, *et al.*, 2017, Comparison of Skeletal Stability after Sagittal Split Ramus Osteotomy among Mono-Cortical Plate Fixation, Bi-Cortical Plate Fixation, and Hybrid Fixation using Absorbable Plates and Screws. *J Craniomaxillofac Surg*, 45:178–82. https://doi.org/10.1016/j.jcms.2016.11.007
19. Gong M, Zhao Q, Dai L, *et al.*, 2018, Fabrication of Polylactic Acid/Hydroxyapatite/Graphene Oxide Composite and their Thermal Stability, Hydrophobic and Mechanical Properties. *J Asian Ceram Soc*, 5:160–8. https://doi.org/10.1016/j.jascer.2017.04.001
20. Nikzad M, Masood SH, Sbarski I, 2011, Thermo-Mechanical Properties of a Highly Filled Polymeric Composites for Fused Deposition Modeling. *Mater Des*, 32:3448–56. https://doi.org/10.1016/j.matdes.2011.01.056
21. Huang G, Du Z, Yuan Z, *et al.*, 2018, Poly(L-Lactide) Nanocomposites Containing Poly (D-Lactide) Grafted Nanohydroxyapatite with Improved Interfacial Adhesion Via Stereocomplexation. *J Mech Behav Biomed Mater*, 78:10–9. https://doi.org/10.1016/j.jmbbm.2017.10.036
22. Shikinami Y, Matsusue Y, Nakamura T, 2005, The Complete Process of Bioresorption and Bone Replacement Using Devices Made of Forged Composites of Raw Hydroxyapatite Particles/Poly L-Lactide (F-u-HA/PLLA). *Biomaterials*, 26:5542–51. https://doi.org/10.1016/j.biomaterials.2005.02.016
23. Takayama T, Todo M, Takano A, 2009, The Effect of Bimodal Distribution on the Mechanical Properties of Hydroxyapatite Particle Filled Poly (L-Lactide) Composites. *J Mech Behav Biomed Mater*, 2:105–12. https://doi.org/10.1016/j.jmbbm.2008.06.001
24. Nejati E, Firouzdor V, Eslaminejad MB, *et al.*, 2009, Needle-Like Nano Hydroxyapatite/Poly(L-Lactide Acid) Composite Scaffold for Bone Tissue Engineering Application. *Mater Sci Eng C*, 29:942–9. https://doi.org/10.1016/j.msec.2008.07.038
25. Gao X, Qi S, Kuang X, *et al.*, 2021, Fused Filament Fabrication of Polymer Materials: A Review of Interlayer Bond. *Addit Manuf*, 37:101658. https://doi.org/10.1016/j.addma.2020.101658
26. Mohan N, Senthil P, Vinodh S, *et al.*, 2017, A Review on Composite Materials and Process Parameters Optimisation for the Fused Deposition Modelling Process. *Virtual Phys Prototyp*, 12:47–59. https://doi.org/10.1080/17452759.2016.1274490
27. Bardiya S, Jerald J, Satheeshkumar V, 2021, The Impact of Process Parameters on the Tensile Strength, Flexural Strength and the Manufacturing Time of Fused Filament Fabricated (FFF) Parts. *Mater Today Proc*, 39:1362–6. https://doi.org/10.1016/j.matpr.2020.04.691
28. Lepoivre A, Levy A, Boyard N, *et al.*, 2021, Coalescence in Fused Filament Fabrication Process: Thermo-Dependent Characterization of High-Performance Polymer Properties. *Polym Test*, 98:107096. https://doi.org/10.1016/j.polymertesting.2021.107096
29. Rao Y, Wei N, Yao S, *et al.*, 2021, A Process-Structure-Performance Modeling for Thermoplastic Polymers Via Material Extrusion Additive Manufacturing. *Addit Manuf*, 39:101857. https://doi.org/10.1016/j.addma.2021.101857
30. Pei N, Hao Z, Wang S, *et al.*, 2021, 3D Printing of Layered Gradient Pore Structure of Brain-like Tissue. *Int J Bioprint*, 7:359–9. https://doi.org/10.18063/ijb.v7i3.359
31. Porter JH, Cain TM, Fox SL, *et al.*, 2018, Influence of Infill Properties on Flexural Rigidity of 3D-Printed Structural Members. *Virtual Phys Prototyp*, 14:148–59. https://doi.org/10.1080/17452759.2018.1537064
32. Kerekes TW, Lim H, Joe WY, *et al.*, 2019, Characterization of Process-Deformation/Damage Property Relationship of Fused Deposition Modeling (FDM) 3D-Printed Specimens. *Addit Manuf*, 25:532–44. https://doi.org/10.1016/j.addma.2018.11.008
33. Yao T, Zhang K, Deng Z, *et al.*, 2020, A Novel Generalized Stress Invariant-Based Strength Model for Inter-Layer Failure of FFF 3D Printing PLA Material. *Mater Des*, 193:108799. https://doi.org/10.1016/j.matdes.2020.108799
34. Popescu D, Zapciu A, Amza C, *et al.*, 2018, FDM Process

Parameters Influence Over the Mechanical Properties of Polymer Specimens: A Review. *Polym Test*, 69:157–66. https://doi.org/10.1016/j.polymertesting.2018.05.020

35. Sharafi S, Santare MH, Gerdes J*, et al.*, 2021, A Review of Factors that Influence the Fracture Toughness of Extrusion-Based Additively Manufactured Polymer and Polymer Composites. *Addit Manuf*, 38:101830. https://doi.org/10.1016/j.addma.2020.101830

36. Costa SF, Duarte FM, Covas JA, 2017, Estimation of Filament Temperature and Adhesion Development in Fused Deposition Techniques. *J Mater Process Technol*, 245:167–79. https://doi.org/10.1016/j.jmatprotec.2017.02.026

Publisher's note